minerals

MDPI

Article

Clinopyroxene Compositions of E-MORB-Type Gabbro from Bingdaban Ophiolites in Central Tianshan, NW China: Insights into the Evolution of the Magmatic System and Geodynamic Setting

Yujia Song [1], Xijun Liu [1,2,3,*], Yao Xiao [1], Xiao Liu [1] and Hao Tian [1]

[1] Guangxi Key Laboratory of Hidden Metallic Ore Deposits Exploration, College of Earth Sciences, Guilin University of Technology, Guilin 541004, China; syj610@glut.edu.cn (Y.S.); xiaoyao@glut.edu.cn (Y.X.); liuxiao@glut.edu.cn (X.L.); nmth521@163.com (H.T.)
[2] Collaborative Innovation Center for Exploration of Nonferrous Metal Deposits and Efficient Utilization of Resource, Guilin University of Technology, Guilin 541004, China
[3] National Key Laboratory of Ecological Security and Resource Utilization in Arid Areas, Xinjiang Institute of Ecology and Geography, Chinese Academy of Sciences, Urumqi 830011, China
* Correspondence: xijunliu@glut.edu.cn; Tel.: +86-152-7739-5399

Abstract: Clinopyroxene, one of the primary rock-forming minerals in mafic rocks, is the major host of lithophile elements in the mantle lithosphere and plays a crucial role in understanding mantle evolution and rock petrogenesis. Taking the Bingdaban ophiolite as an example, this study employed electron probe microanalysis and in situ trace element analysis to investigate the geochemistry of clinopyroxene in gabbros to determine the magma series and evolution, constrain the physicochemical conditions of the magmatic processes and explore the petrogenesis and tectonic setting. Representative gabbro samples were subjected to zircon U–Pb isotopic analysis, yielding an age of 424.3 ± 5.9 Ma. Geochemical investigations revealed that the Bingdaban gabbros exhibit tholeiitic composition, suggesting a genesis associated with enriched mid-ocean ridge basalt (E-MORB). Mineralogical analyses indicated that the clinopyroxene in the gabbros was Mg-rich, Fe-poor, and alkali-poor, representing a subalkaline series. The compositional end members of clinopyroxene were calculated as $Wo_{38.9–48.0}En_{30.9–48.1}Fs_{10.4–24.4}$, indicating a predominance of diopside with a minor amount of augite. Temperature–pressure conditions imply that these rocks formed in a high-temperature, low-pressure, and shallow-source environment. Compositional estimates of the melt in equilibrium with clinopyroxene are consistent with the overall characteristics of the host rock, reflecting an E-MORB setting. The Bingdaban gabbro likely originated from an initially depleted mantle source that later received an input of enriched mantle material, indicating formation in either an initial oceanic or immature back-arc basin tectonic setting.

Keywords: Central Tianshan; Bingdaban ophiolite; clinopyroxene; parental magma; petrogenesis

Citation: Song, Y.; Liu, X.; Xiao, Y.; Liu, X.; Tian, H. Clinopyroxene Compositions of E-MORB-Type Gabbro from Bingdaban Ophiolites in Central Tianshan, NW China: Insights into the Evolution of the Magmatic System and Geodynamic Setting. *Minerals* **2023**, *13*, 1232. https://doi.org/10.3390/min13091232

Academic Editors: Jingsui Yang, Souvik Das, Weiwei Wu and Rubén Díez-Fernández

Received: 9 August 2023
Revised: 11 September 2023
Accepted: 18 September 2023
Published: 20 September 2023

1. Introduction

Suture zones serve as indicators of subduction–collision tectonics, where the closure of ocean and back-arc basins occurs [1]. These zones are highly deformed belts representing locations where former ocean basins were destroyed. An orogenic suture refers to a high-strain zone containing fragmented remnants of ophiolite and blueschist mélanges. Ophiolites are fragments of the obducted oceanic lithosphere exposed on the continental crust. Suture zones exhibit characteristic features that preserve a record of tectonic and magmatic processes from the rift–drift phase to the accretionary and collisional stages of continental margin evolution in various tectonic settings [2,3], and ophiolites developed cin these settings can be classified into various types, including suprasubduction zone (SSZ), mid-ocean ridge (MOR), continental margins, volcanic arc, accretionary, and plumes [3,4].

The Tianshan Orogenic Belt was formed during the Paleozoic as a result of the subduction of the Junggar and Paleo-Tianshan oceans, along with the accretion of Precambrian crustal fragments or microcontinents, Paleozoic island arcs, ophiolites, and accretionary complexes [5,6]. As a Late Paleozoic collisional and accretionary orogen, the Tianshan Orogenic Belt underwent two major stages of N–S accretion and/or collision during the Paleozoic [7–9], followed by a strong influence from subsequent large-scale strike–slip faults. These faults are distributed in an E–W direction along the Gangou-Mishigou-Wusutongou-Bingdaban ophiolite, representing a subduction-related accretionary complex formed during the southward subduction of the North Tianshan Ocean [10].

The Bingdaban ophiolite mélange is a major ophiolite belt that preserves the remnants of the ancient Tianshan oceanic crust within the Central Tianshan suture zone. Previous studies have primarily focused on the petrogeochemical characteristics and tectonic environment of ophiolites. Dong et al. [11] identified MORB–type ophiolites and subduction-related volcanic rocks in the tectonic mélange of the Gangou–Wusutong section in Central Tianshan, providing direct evidence for the existence of the Bingdaban ophiolite mélange and its role in subduction. Liu et al. [12] obtained Late Permian ages of ca 265.2 $\pm$ 1.8 Ma for N-MORB basalts and Silurian ages of ca 425.4 $\pm$ 3.9 Ma for E-MORB signatured diabase, respectively, indicating the presence of an ocean basin in the northern margin of the Central Tianshan during the Late Permian and Late Silurian. However, because of the later tectonic dissection, deformation, and metamorphism that the ophiolite in the region has undergone, it is not sufficient to assess its petrogenesis based solely on whole-rock geochemical composition of the altered rocks.

To comprehensively analyze petrogenesis by combining mineralogical geochemistry with whole-rock geochemical analysis, this study conducted whole-rock geochemical analysis and zircon U–Pb dating of gabbro samples from the Bingdaban ophiolite mélange and performed in situ major–trace element geochemical analysis of clinopyroxene for the first time. Clinopyroxene phenocrysts are resistant to low-grade metamorphism and postmagmatic processes, and their compositions reflect the host magma type [13]. As such, clinopyroxene phenocrysts are important petrogenetic archives of the compositional evolution of magmas, the thermochemical state of magmatic systems, and the tectonic setting of magmatism. Based on petrographic and whole-rock geochemical analyses, this study presents the first mineralogical and mineral chemical characterization of clinopyroxene in gabbros from Bingdaban on the northern margin of Central Tianshan. This study performed clinopyroxene–melt equilibrium calculations to estimate the parental magma composition, exploring the physicochemical conditions of magma properties, origin, and evolutionary processes, providing valuable constraints on the tectonic setting of the Bingdaban basic magmatic system in Central Tianshan.

2. Geological Background and Sample Description

The Tianshan Orogenic Belt, which extends approximately 2500 km from northwest China in the east to Central Asia in the west (Figure 1a), is situated along the southwest margin of the Central Asian Orogenic Belt (CAOB) and it is sandwiched between the Tarim Basin to the south and the Junggar Basin to the north [14], with its western boundary adjacent to Kazakhstan [15–17] (Figure 1b). It represents a Paleozoic orogenic collage formed by multiple subductions and accretions of various microcontinents and magmatic arcs [18], seamounts, and accretionary complexes in the Late Paleozoic, following the closure of the Junggar Ocean to the north and the Southern Tianshan Ocean to the south [15,19]. The Tianshan Orogenic Belt in the north–south direction can be divided into three parts: northern, central, and southern Tianshan, by the Bingdaban and Wuwamen faults (Figure 1c), based on their distinctive rock assemblages, geological features, and tectonic evolution [9,11,15,16,20,21].

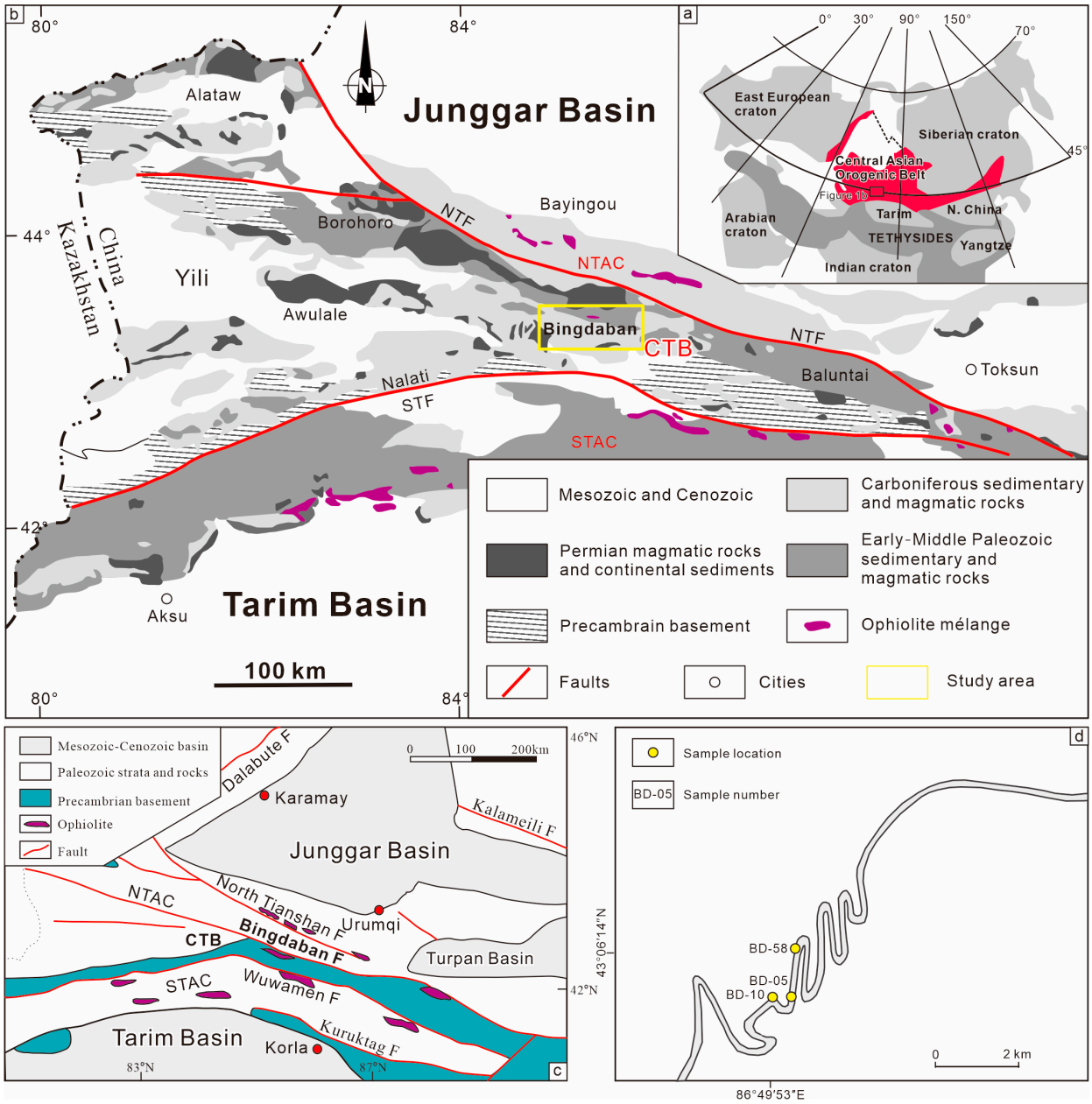

Figure 1. (**a**) Map of the Central Asian Orogenic Belt (CAOB) and surrounding cratons [22]; (**b**) map showing the tectonic framework of the Tianshan Orogenic Belt [15]; (**c**) simplified geological map of the Central Tianshan Block showing the main tectonic boundaries of Bingdaban [23]; (**d**) sample locations. CTB: Central Tianshan Block, NTAC: North Tianshan accretionary complex, STAC: South Tianshan accretionary complex, NTF: North Tianshan Fault, STF: South Tianshan Fault.

The western segment of the Tianshan Orogenic Belt in China intersects with the Yili terrane (Figure 1b), which is associated with the Central Tianshan microcontinent and sandwiched between the Northern and Central–Southern Tianshan suture zones. The North Tianshan suture zone corresponds to the closure of the Paleozoic North Tianshan Ocean, characterized by a series of Early Paleozoic ophiolites and associated rock assemblages in the Tangbale, Bingdaban, and Gangou regions [24], further connecting eastward with the Kangguertage ophiolite. The Central–Southern Tianshan suture zone is thought to have formed from the closure of the Southern Tianshan Ocean and marginal seas, consisting of the Changawuzi, Guluogou, Wuwameng, and metamorphosed Yushugou ophiolites from west to east [8,15,25].

The study area is located in the Bingdaban region on the northern margin of Central Tianshan. The exposed rocks are located between Hongwuyueqiao and Glacier No. 1 on the northern side of the Bingdaban peak [12]. Based on the 1:200,000 geological map [26], Bingdaban consists primarily of two sets of rock assemblages: a mélange matrix and ophiolitic tectonic remnants. The mélange matrix is predominantly composed of Paleozoic intrusive rocks, including deformed granodiorite, undeformed porphyritic granite, quartz diorite, and andesite diorite, which have been affected by late ductile shear deformation and commonly exhibit varying degrees of mylonitization [27,28]. Similar to other typical ophiolites, the Bingdaban ophiolite has been dissected and exists as individual tectonic blocks with relatively complete ophiolitic rock sequences. These tectonic blocks are mainly exposed in the north of Wangfengdaoban, and are mainly composed of gabbro, diabase, and basalt tectonic blocks, which are bound in a hybrid matrix composed of volcanic and sedimentary rock series to form a mélange belt, and have been transformed by low-grade greenschist to greenschist facies metamorphism.

Five gabbro samples (Tables S1 and S2, Supplementary Materials) are selected in this study. One gabbro sample (BD-10) was selected for zircon U–Pb dating (GPS: 86°49′52″ E, 43°05′38″ N). Three gabbro samples (BD-05, BD-10, and BD-58; Figure 1d) were collected from the Bingdaban ophiolite for geochemical analyses, and were specifically collected from the freshest outcrops observed at each respective locality. The whole-rock data of two gabbro rocks (BD-88; BD-100) were obtained from Liu et al. [29], and their mineral chemistry was analyzed in this paper. Gabbros are dark greenish–green, medium-grained blocky structures (Figure 2a–d). The primary rock-forming minerals were euhedral to subhedral clinopyroxene and plagioclase, exhibiting ophitic texture, with clinopyroxene comprising 50–60 vol.% and plagioclase comprising 30–40 vol.%, along with a small amount of Fe–Ti oxides (<10 vol.%) (Figure 3a–b). The clinopyroxene crystals showed no zoning in the backscattered electron (BSE) images (Figure 3c–d), and several clinopyroxene grains exhibited cracks, whereas plagioclase phenocrysts appeared as tabular grains.

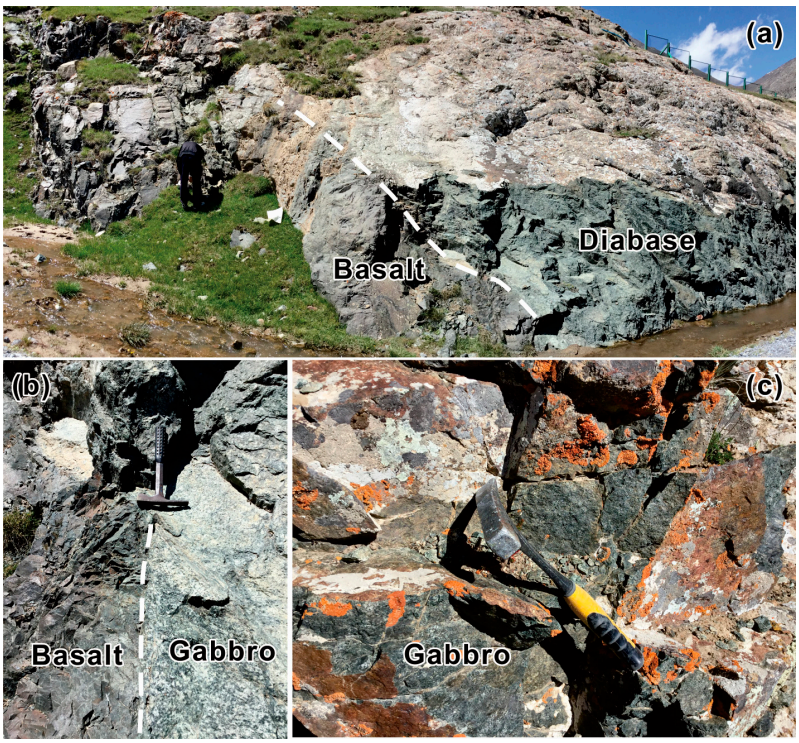

Figure 2. Representative field photographs of the Bingdaban ophiolite. (**a**,**b**) Contact boundary between the Bingdaban basalt and diabase, and (**c**) outcrops of Bingdaban gabbro.

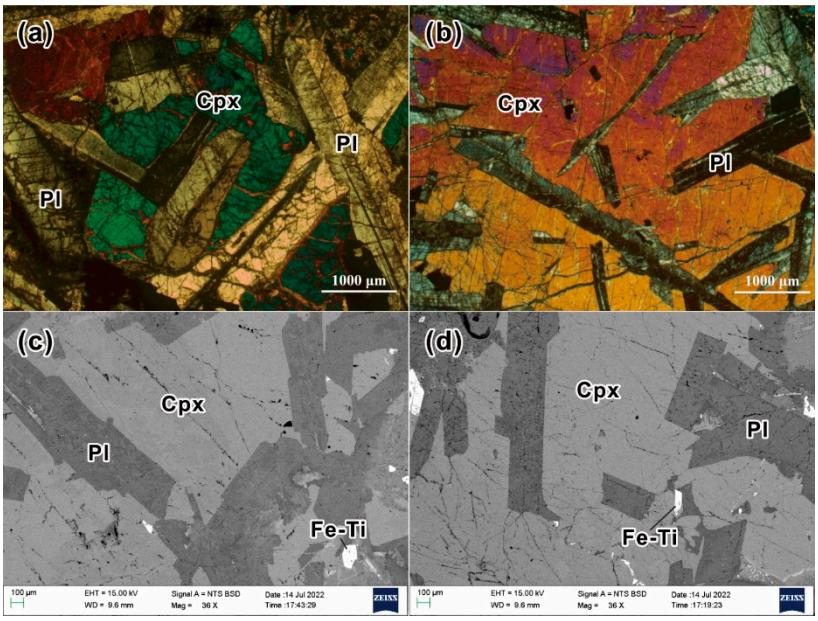

Figure 3. (**a**,**b**) Photomicrographs showing the major minerals and textures of the Bingdaban gabbro; medium-grained texture of gabbro. (**c**,**d**) Backscattered electron (BSE) images of clinopyroxene grains in the Bingdaban gabbro (Pl = plagioclase, Cpx = clinopyroxene, Fe–Ti = iron–titanium oxides).

3. Analytical Methods

All the different types of analyses were undertaken at the Guangxi Key Laboratory of Hidden Metallic Ore Deposits Exploration, Guilin University of Technology, Guangxi, China.

3.1. Zircon Geochronology

The zircon grains were separated from the samples using crushing, heavy liquid, and magnetic separation techniques before being handpicked under a binocular microscope. The zircons were mounted in epoxy resin discs and polished to approximately half their grain thickness. All zircon grains were documented with transmitted and reflected light photomicrographs, as well as cathodoluminescence (CL) images from an electron microprobe (JXA8230R) to reveal internal structures. The detailed operating conditions of the laser ablation inductively coupled plasma mass spectrometry (LA-ICP-MS) and data reduction procedures are described by Liu et al. [29] and Song et al. [30]. The laser spot size and frequency were set to 32 μm and 6 Hz, respectively. The NIST610 glass standard was used as an external standard for U–Pb dating and trace element analysis. Zircon standard GJ–1 was also used as a secondary standard to assess the data quality. Concordia ages and diagrams were obtained using Isoplot/Ex (3.0) software [31].

3.2. Whole-Rock Major and Trace Elements

Fresh samples were crushed, and the chips were soaked in 4 N HCl for 30 min to remove alteration minerals. Rock chips were powdered using an alumina ceramic shatterbox. Prior to major element analyses, loss on ignition (LOI) values were measured after heating in a muffle furnace at a constant temperature of 1000 °C. The baked samples were then fused into glass disks with $Na_2B_4O_7{\cdot}10H_2O$ at ~1150 °C, and an ZSX Primus II X-ray fluorescence spectrometer was used to determine the major element compositions. Trace element compositions were determined with an Agilent 7500cx ICP-MS. The precisions of the major and trace element analyses were better than ±2–5%. During the analyses, United Stated Geological Survey (USGS) standards BHVO-2, AGV-2, W-2, and G-2 and Chinese national rock standards GSR-1, -2, and -3 were used to obtain the measured elemental concentrations.

3.3. Mineral Chemistry

This study analyzed fresh clinopyroxene grains ranging from euhedral to subhedral in shape, with grain sizes between 0.5 and 2.0 mm. The major elemental contents of the minerals were determined using a JEOL JXA-8230 electron probe microanalysis (EPMA) equipped with four wavelength-dispersive spectrometers (WDSs). The analyses were performed at a 15 kV accelerating voltage, 20 nA probe current, and 1 μm electron beam diameter. The dwell times were 10 s for the elemental peaks and 5 s for both sides of the peaks. Raw X-ray intensities were corrected using ZAF (atomic number, absorption, and fluorescence) correction procedures.

Trace element analyses were conducted using LA-ICP-MS with an Agilent 7900 quadrupole ICP-MS coupled to a photon machine analyte HE 193 nm ArF excimer LA system. A squid signal-smoothing device is part of this LA system. During the measurements, He was used as the carrier gas. Each analysis used a spot diameter of 30 μm, laser repetition rate of 8 Hz, and laser energy of 4 J/cm^2. Data were acquired during ablation for 40 s, after measuring the gas blank for 20 s. Standard reference glasses SRM 610, SRM 612, and BCR-2G were used as external standards to correct for mass discrimination and time-dependent drift. For most major and trace elements, the analytical accuracy and precision were greater than ±10%.

4. Results

4.1. Zircon U–Pb Geochronology

Zircon grains from the studied sample (BD-10) are euhedral to subhedral with prismatic or granular shapes and crystal lengths of 50–200 μm. The CL images of zircons show oscillatory or striped zonation, and appear to be of igneous origin. The isotopic ratios and age results are presented in Table S1 and Figure 4, respectively. Nine valid data points were obtained after correction, with Th/U values ranging from 0.15–0.82. Most of the ratios are greater than 0.4, which is consistent with the characteristics of magmatic zircons. The weighted average age of the nine grain analyzed points based on the $^{206}Pb/^{238}Pb$ value is 424.3 ± 5.9 Ma (n = 9, MSWD = 0.112), representing the Late Silurian age of the gabbro formation.

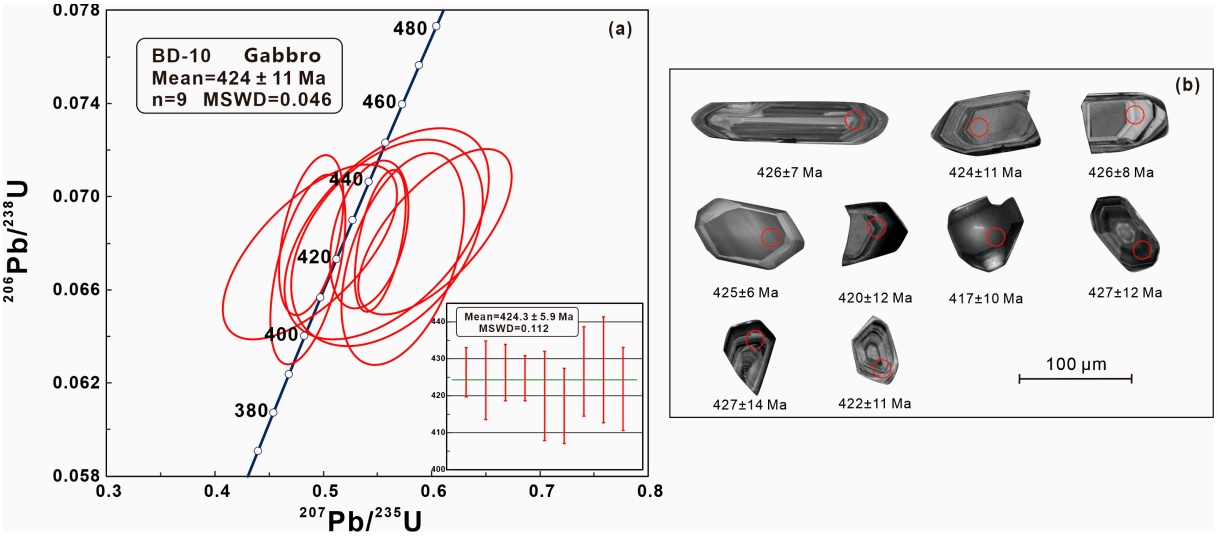

Figure 4. (**a**) Zircon U–Pb concordia diagram and $^{206}Pb/^{238}U$ weighted mean ages of the Bingdaban gabbro; (**b**) zircon cathodoluminescence (CL) images.

4.2. Major and Trace Elements

Five representative gabbro samples from the Bingdaban ophiolite mélange were selected for whole-rock major–trace element analysis; the results are presented in Table S2.

LOI values ranged from 0.76–3.00 wt.%. The major oxides were normalized to 100 wt.% on an anhydrous basis. The rock geochemical analysis results showed that the gabbros had relatively high SiO_2 content, ranging from 48.87–51.66 wt.%, and high MgO content, ranging from 6.15–8.63 wt.%, with high $Mg^{\#}$ values ranging from 55–68, slightly lower than the initial magma $Mg^{\#}$ values (68–75). The TiO_2 content ranges from 1.33 to 2.33 wt.%, with an average of 1.82 wt.%, close to the TiO_2 content of MORB (1.5 wt.%). The Al_2O_3 content ranges from 15.28 to 17.60 wt.%, with an average of 16.21 wt.%, similar to MORB with an Al_2O_3 content of 16.2 wt.%. The K_2O (0.37–1.26 wt.%), Na_2O (2.58–3.96 wt.%), and $Na_2O + K_2O$ contents (3.02–4.33 wt.%) are relatively low.

In the total alkali-silica (TAS) diagram (Figure 5a), the samples are distributed within the subalkaline gabbro and/or basalt range and fall within the field of the tholeiitic basalt series in the SiO_2–FeO^T/MgO diagram (Figure 5b).

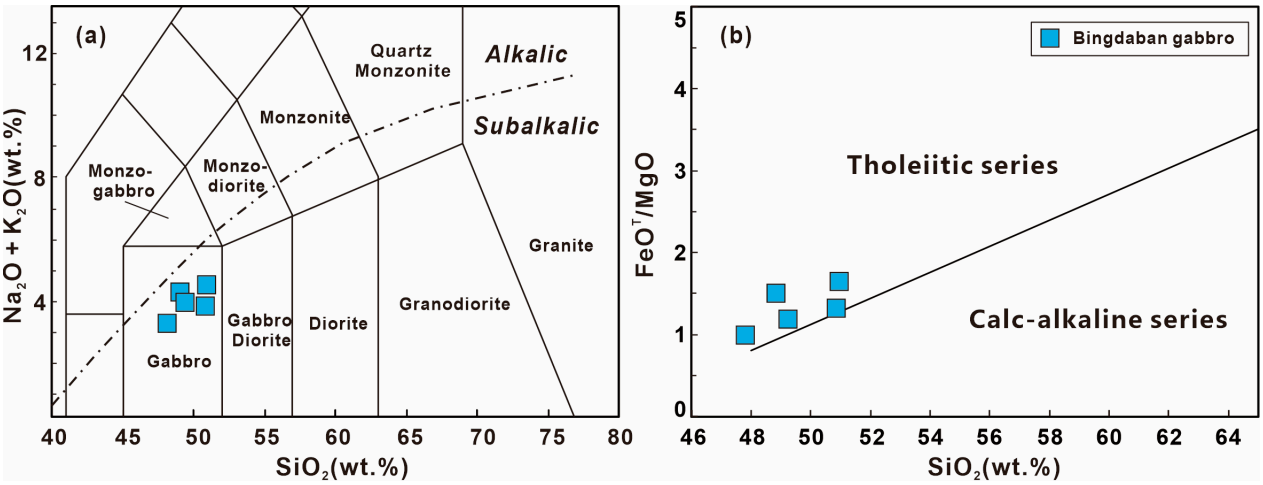

Figure 5. (**a**) Total alkali-silica (TAS) classification diagram [32]; (**b**) FeO^T/MgO–SiO_2 diagram [33].

The gabbros had low total rare-earth element (ΣREE) contents (36–99 ppm), with an average of 61 ppm, which is comparable to the E-MORB value (49 ppm) reported by Sun and McDonough [34]. Light and heavy REEs (LREEs and HREEs) exhibit no significant fractionation, with $(La/Yb)_N$ values ranging from 1.13–2.76. The chondrite-normalized distribution pattern exhibits weak enrichment in LREEs and relatively flat distribution for HREEs, with a weak Eu anomaly (δEu = 0.95–1.38), forming a nearly straight line (Figure 6a), indicating its genesis in an E-MORB environment. All gabbro samples had $(Rb/Yb)_N$ values greater than 1. In the primitive-mantle-normalized trace element diagrams (Figure 6b), apart from the significant positive anomalies of Rb, U, Pb, Sr, Zr, and Hf, the overall enrichment of the high-field-strength elements (HFSE) is comparable to that of E-MORB.

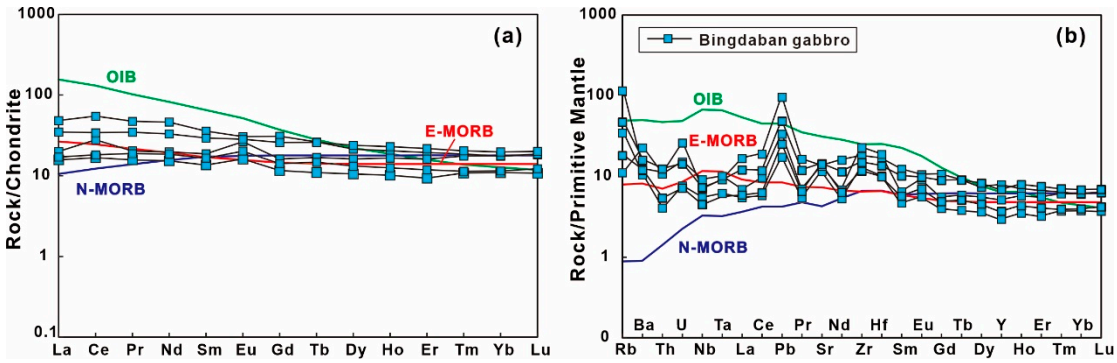

Figure 6. (**a**) Chondrite-normalized rare-earth element (REE) patterns and (**b**) primitive-mantle-normalized trace element spider diagrams. Normalizing values are from Sun and McDonough [34].

4.3. Mineral Chemistry

Major and trace element data for clinopyroxene phenocrysts in the Bingdaban gabbro are presented in Tables S3 and S4, where no complex structural features or compositional zoning were observed in the clinopyroxene. According to the clinopyroxene classification scheme proposed by Morimoto [35], the clinopyroxene in the Bingdaban gabbro belongs to the Ca–Mg–Fe clinopyroxene group (Figure 7). In the Wo–En–Fs triangular diagram (Figure 8), the clinopyroxene grains in the Bingdaban gabbro were predominantly diopside and augite, with compositions ranging from $Wo_{38.9–48.0}En_{30.9–48.1}Fs_{10.4–24.4}$. Clinopyroxene exhibited a relatively high MgO content, with $Mg^{\#}$ values ranging from 60 to 82, with an average of 73. High levels of CaO (19.41–22.25 wt.%) and FeO (6.35–13.65 wt.%, relatively low levels of Al_2O_3 (1.44–3.41 wt.%) and Na_2O (0.19–0.69 wt.%), and scattered TiO_2 contents (0.28–2.24 wt.%) were also observed.

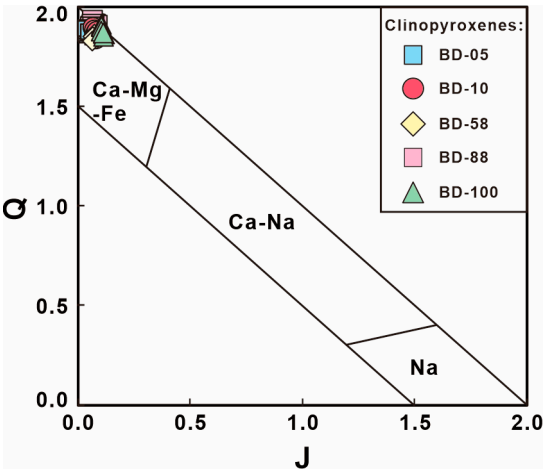

Figure 7. Diagram of Q–J series for clinopyroxenes [35]. Q = n (Ca) + n (Mg) + n (Fe^{2+}); J = 2n (Na).

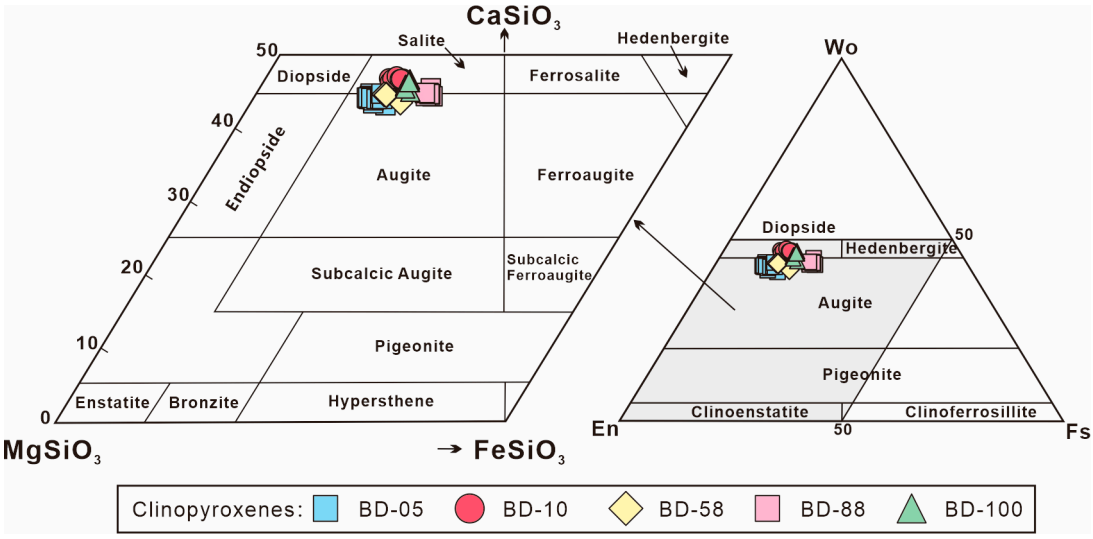

Figure 8. Diagrams of clinopyroxenes classification [35]; Wo—diopside, En—enstatite, Fs—ferrosilite.

The ∑REE content was relatively low, ranging from 15.9 to 116 ppm. The $(La/Sm)_N$ and $(La/Yb)_N$ values range from 0.14–0.61 and 0.16–0.62, respectively, indicating that the LREEs are significantly depleted compared to the middle REEs (MREEs) and HREEs. This suggests a convex-upward trend for the MREEs and concave-downward trend for LREEs and HREEs. Additionally, there were negative Eu anomalies (Eu/Eu* = 0.45–1.0), with a particularly strong negative Eu anomaly observed in samples BD–05 and BD–88. Overall,

the samples exhibit a convex-upward pattern in their REE distributions (Figure 9a,c,e,g,i). In the trace element patterns normalized to the primitive mantle (Figure 9b,d,f,h,j), the clinopyroxene showed a significant depletion in Nb and Sr, as well as a weak depletion in Zr and Hf.

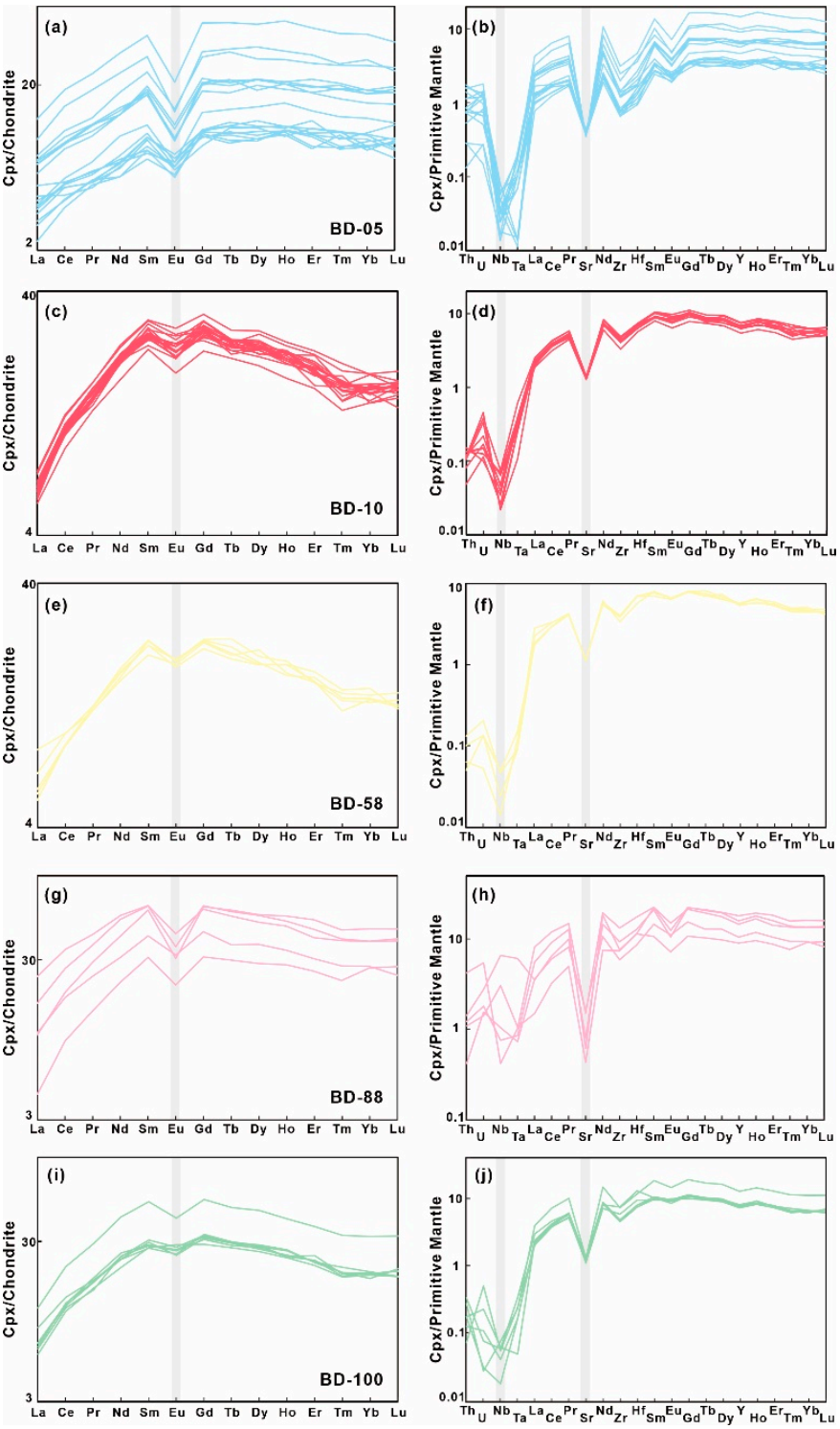

Figure 9. (**a**,**c**,**e**,**g**,**i**) Chondrite-normalized REE patterns and (**b**,**d**,**f**,**h**,**j**) primitive-mantle-normalized incompatible element patterns of clinopyroxene grains from Bingdaban gabbro. The normalization values data are from Sun and McDonough [34].

5. Discussion

5.1. Magma Series

Previous studies [36–38] have indicated that the composition of clinopyroxene is influenced by the composition of the parent magma and its crystallization environment. Therefore, if the magma source undergoes mixing, clinopyroxene phenocrysts can reflect the compositional characteristics of the parent magma more accurately than the whole-rock composition. The incompatible nature of Si and Al in igneous rocks makes their combination an important proxy for determining the parent magma type [39]. In this study, the clinopyroxene exhibited high SiO_2 and low Al_2O_3, K_2O, and Na_2O contents, indicating that the parent magma of the host rock is a subalkaline series. In the SiO_2–Al_2O_3 diagram of clinopyroxene (Figure 10a), the majority of clinopyroxenes fall within the subalkaline rock field, with only a few samples falling at the boundary between the subalkaline and alkaline rock fields. Furthermore, in the Si–Al diagram of clinopyroxene (Figure 10b), all clinopyroxene samples fall within the field of the tholeiitic basalt series. Additionally, in the Al_2O_3–Na_2O–TiO_2 and SiO_2–Na_2O–TiO_2 diagrams (Figure 11), the clinopyroxene samples are located within the tholeiitic basalt series field. Moreover, in the TAS classification diagram for the whole-rock major elements (Figure 5a), all samples fall within the subalkaline gabbro field, whereas in the SiO_2–FeO^T/MgO diagram (Figure 5b), they fall within the tholeiitic basalt series field. In conclusion, the parent magma of the Bindaban gabbro was likely a subalkaline tholeiitic basalt magma.

5.2. Temperatures and Pressures of Magma Formation

Igneous thermobarometers can provide important insights into magma formation. To better understand the melting conditions during the formation of the Bingdaban ophiolite, clinopyroxene–melt thermobarometers were used to calculate the temperatures and pressures of phenocryst crystallization [40,41]. The calculation of the crystallization temperature of clinopyroxene is based on phase equilibria and high-temperature and high-pressure melting experimental data [40,41]. The clinopyroxene–liquid equilibrium constant, $K_D(Fe–Mg)^{cpx/liq}$, can be used to determine whether clinopyroxene is in equilibrium with its host rock. The clinopyroxene was in equilibrium when $K_D(Fe–Mg)^{cpx/liq}$ = 0.2–0.4 [42,43]. We used the equation $K_D(Fe/Mg)^{cpx/liq} = 0.109 + 0.186 \times Mg\#$ cpx proposed by Wood and Blundy [44] to calculate the $K_D(Fe–Mg)^{cpx/liq}$ of the studied clinopyroxene grains, which yielded values of 0.213–0.261 (Table S5), suggesting that the clinopyroxene grains are in equilibrium with their host rocks. As such, the temperatures and pressures calculated from clinopyroxene in the Bingdaban ophiolite robustly constrained the pressure and temperature conditions for clinopyroxene crystallization.

5.3. Temperatures and Pressures of Magma Formation

Igneous thermobarometers can provide important insights into magma formation. To better understand the melting conditions during the formation of the Bingdaban ophiolite, clinopyroxene–melt thermobarometers were used to calculate the temperatures and pressures of phenocryst crystallization [40,41]. The calculation of the crystallization temperature of clinopyroxene is based on phase equilibria and high-temperature and high-pressure melting experimental data [40,41]. The clinopyroxene–liquid equilibrium constant, $K_D(Fe–Mg)^{cpx/liq}$, can be used to determine whether clinopyroxene is in equilibrium with its host rock. The clinopyroxene was in equilibrium when $K_D(Fe–Mg)^{cpx/liq}$ = 0.2–0.4 [42,43]. We used the equation $K_D(Fe/Mg)^{cpx/liq} = 0.109 + 0.186 \times Mg\#$ cpx proposed by Wood and Blundy [44] to calculate the $K_D(Fe–Mg)^{cpx/liq}$ of the studied clinopyroxene grains, which yielded values of 0.213–0.261 (Table S5), suggesting that the clinopyroxene grains are in equilibrium with their host rocks. As such, the temperatures and pressures calculated from clinopyroxene in the Bingdaban ophiolite robustly constrained the pressure and temperature conditions for clinopyroxene crystallization.

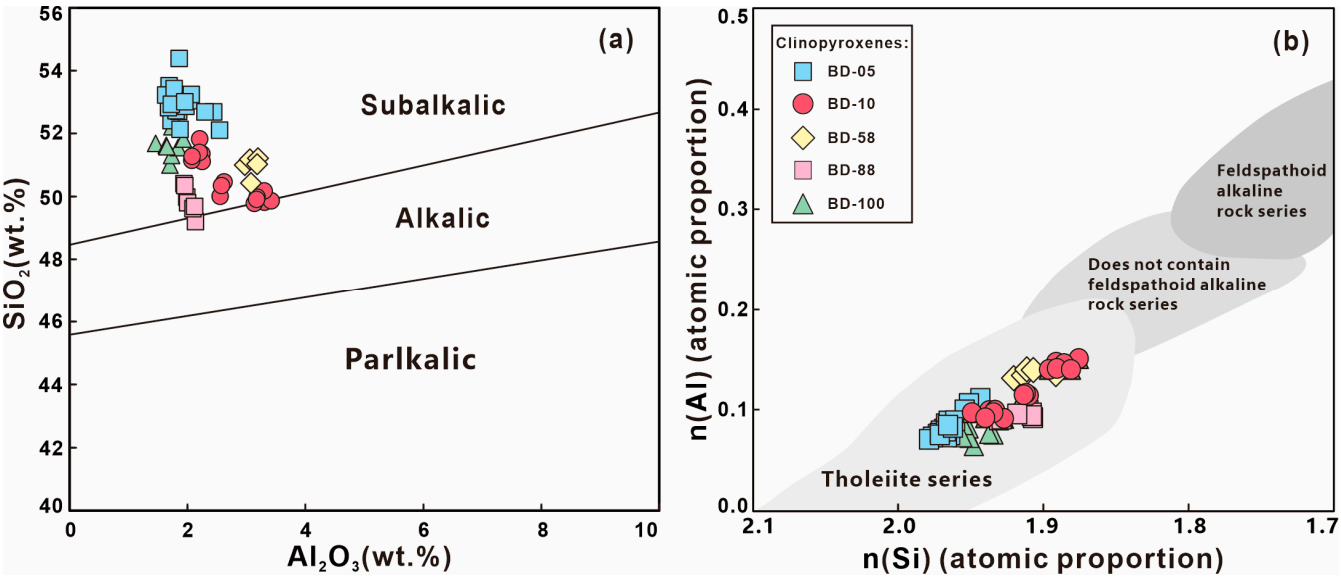

Figure 10. (**a**) SiO_2 vs. Al_2O_3 and (**b**) n(Al) vs. n(Si) of clinopyroxenes from Bingdaban gabbro [36].

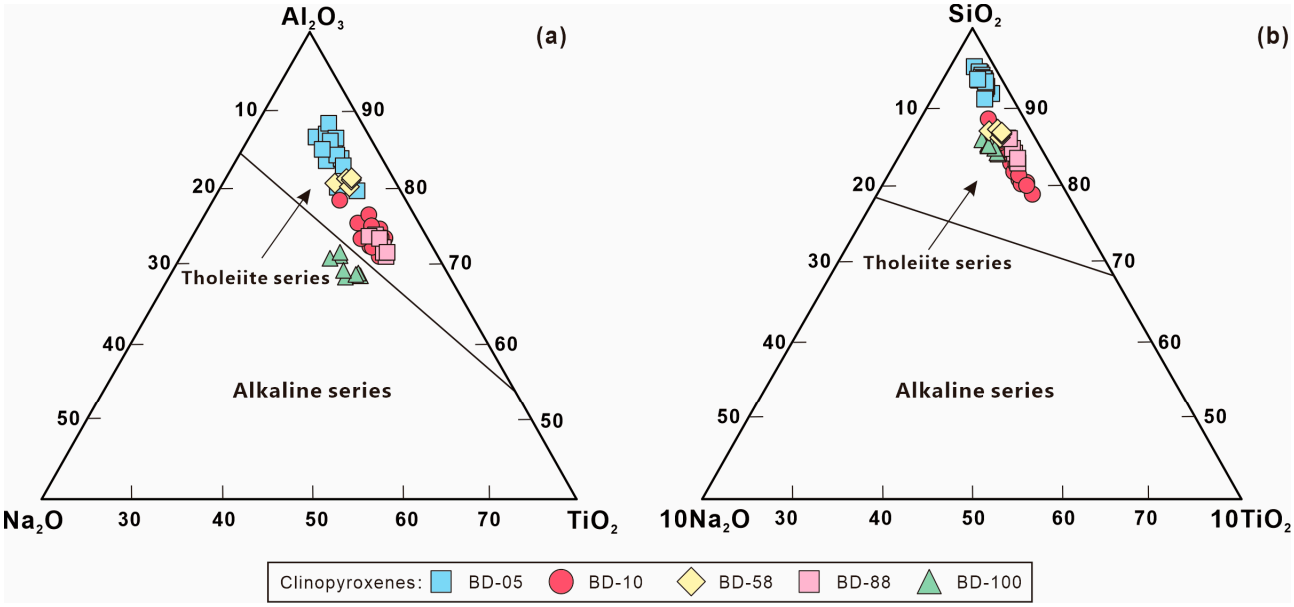

Figure 11. (**a**) Al_2O_3–Na_2O–TiO_2 and (**b**) SiO_2–Na_2O–TiO_2 of clinopyroxenes [36].

Currently, there are various types of clinopyroxene thermobarometers, among which Neave and Putirka [45] established a calculation formula for the clinopyroxene temperature and pressure based on a substantial amount of research and analysis of the equilibrium relationship between clinopyroxene and its host rock. The clinopyroxene–melt equilibrium temperatures and pressures obtained using the above formula are listed in Table S6. Based on the clinopyroxene thermobarometer of Putirka et al. [34], the temperatures of clinopyroxene crystallization varied from 1120–1188 °C (average = 1145 °C), which are slightly lower than the temperature of the asthenospheric mantle (1280–1350 °C). The crystallization pressure was 0.1–0.8 GPa (average = 0.4 Gpa), corresponding to crystallization depths of 4–25 km (average depth = 12 km; based on 1 Gpa = 33 km) [41].

The large variation in clinopyroxene phenocryst crystallization depths suggests that these phenocrysts did not form through a single crystallization event in a magma chamber at a specific depth, but, rather, crystallized continuously during the ascent of the magma. The crystallization conditions of clinopyroxene reflect the nonadiabatic nature of

the magma ascent process, indicating thermal dissipation (Figure 12). The relatively large size, homogeneous chemical composition, and absence of zoning structures in the studied clinopyroxene phenocrysts suggest that the crystallization process was extremely slow. The good linear correlation among the major elements implies that the clinopyroxene particles formed in a relatively stable magma chamber or magma evolution. In other words, the clinopyroxenes in the Bingdaban gabbro and its host rock were in a state of equilibrium, and all samples were formed by varying degrees of fractional crystallization from the same parent magma, indicating that they were products of early crystallization.

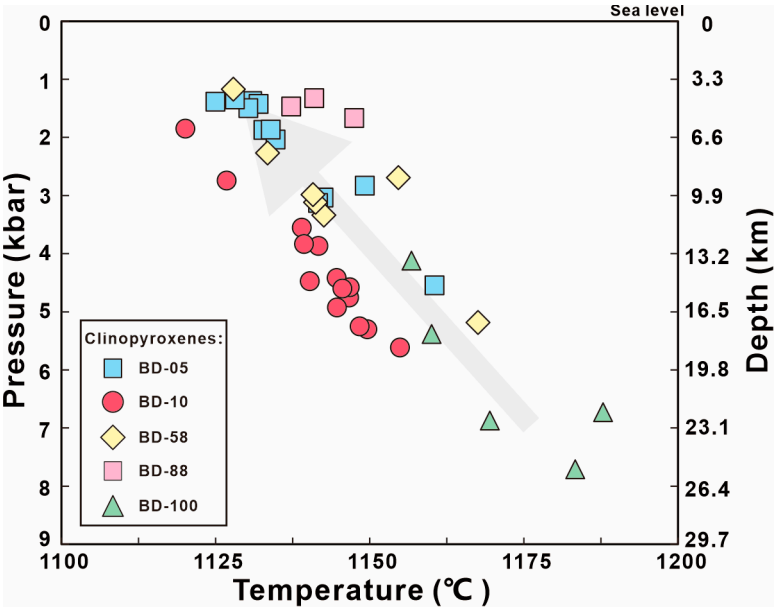

Figure 12. Clinopyroxene–melt equilibrium thermobarometry models for Bingdaban gabbro [40].

In clinopyroxene, the coordination of Al is closely related to temperature and pressure and has important implications for magma crystallization and differentiation. During the magmatic evolution from high to low temperatures, the coordination of Al increased from hexacoordinated to tetracoordinated [38]. Similarly, from the mantle to the crust, Al transitioned from hexacoordinated to tetracoordinated as the pressure decreased. In the study area, Al^{IV} ranged from 0.0003 to 0.1635, with an average of 0.0709, whereas Al^{VI} ranged from 0.0015 to 0.0603, with an average of 0.0195. The relatively high ratio of Al^{IV} to Al^{VI} indicates that the rock suite formed under relatively high-temperature and low-pressure conditions [7], which aligns with the temperature and pressure estimates based on Neave and Putirka [45]. Clinopyroxene is the primary rock-forming mineral in gabbro and crystallizes early. Therefore, the crystallization temperature and pressure of clinopyroxene represent the temperature and pressure conditions during the formation of the Bingdaban gabbro.

5.4. Equilibrium Parental Magma Compositions

Under equilibrium conditions, the major and trace element compositions of clinopyroxene can be used to infer the composition of the melt in equilibrium with clinopyroxene. The $Mg^{\#}$ value of the melt in equilibrium with clinopyroxene can be estimated using the Fe and Mg partition coefficients between the two. Utilizing the partition coefficient K_d^{cpx} [$K_d^{cpx} = (w_{FeO}/w_{MgO})_{cpx}/(w_{FeO}/w_{MgO})_{liq}$] = 0.36 ± 0.04 [46], where cpx represents clinopyroxene and liq represents melt, we estimated the $Mg^{\#}$ value of the magma in equilibrium with clinopyroxene to be 31–62 (with an average of 48). Comparing the calculated $Mg^{\#}$ values of the primitive magma with the $Mg^{\#}$ value of the host rock, the $Mg^{\#}$ values of the samples (BD-05, BD-10, and BD-58) calculated for the primitive magma were similar to the $Mg^{\#}$ values of the host rock (Table S3). However, compositional differences exist among

cogenetic clinopyroxenes, which can be attributed to the heterogeneity of the initial melt and variations in the melt composition due to fractional crystallization and magma mixing.

Under equilibrium conditions, the trace element composition of the melt in equilibrium with clinopyroxene can be calculated using the trace element composition of clinopyroxene and mineral–melt partition coefficients (Table S5). We utilized the mineral–melt partition coefficients from Hart and Dunn [47] to estimate the trace element composition of the primary melt of the Bindaban gabbro. The changes in the concentration of trace elements in clinopyroxene during the process of fractional crystallization were determined using the Rayleigh fractionation equation, $X_i = K_D \times Xi0 \times F^{(K_D - 1)}$, where X_i and Xi 0 represent the concentrations of trace elements in the host rock and primary melt, respectively, and F represents the percentage of initial magma left after fractional crystallization. In this model, we selected clinopyroxene crystals from the gabbro samples (BD-05, BD-10, and BD-58) that have low ∑REE values (Table S3) and are in equilibrium with their host rock. The calculated $Mg^{\#}$ values of the primitive magma were similar to the $Mg^{\#}$ values of the host rock, serving as the starting melt for fractional crystallization calculations (Figure 13).

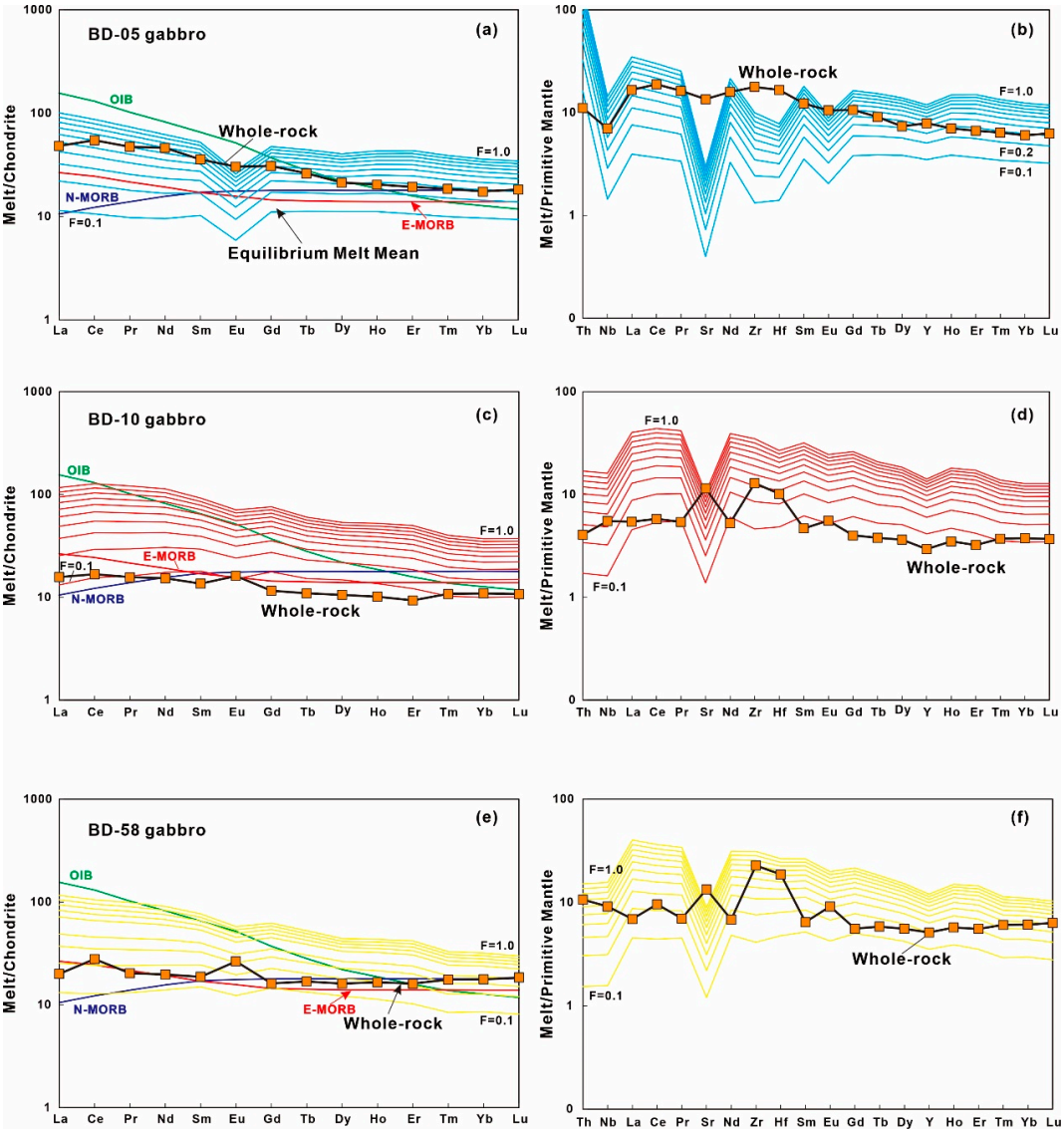

Figure 13. Simulated calculations of chondrite-normalized REE patterns (**a**,**c**,**e**) and primitive-mantle-normalized incompatible element patterns (**b**,**d**,**f**) of equilibrated melts with clinopyroxenes from the Bingdaban gabbro. The normalization data are from Sun and McDonough [34].

As shown in Figure 13, the estimated melt in equilibrium with clinopyroxene exhibited a relatively high abundance of trace elements, with most being higher than the host whole-rock composition. The normalized multielement diagram shows a weak enrichment of LREEs and relative flatness of HREEs. The primitive-mantle-normalized diagram exhibits a weak depletion of HFSEs (such as Nb, Zr, and Hf), reflecting the genetic characteristics of E-MORB environments similar to the host rock. By comparing the equilibrium melt composition with the whole-rock composition, it is estimated that 50–90% of the initial magma underwent fractional crystallization during clinopyroxene crystallization. Overall, the calculated melt model is similar to the E-MORB and host whole-rock melt models.

5.5. Petrogenesis of E-MORB Gabbro

The origin of E-MORB has attracted significant attention because it may reflect variations in the source composition and degrees of mixing, melting, and fractional crystallization, as well as the influence of alteration processes [48,49]. Discussion on the origin of E-MORB is primarily based on studies of modern ocean basins. Based on the differences in major and trace element enrichment, previous studies have classified MORB-type rocks into two main categories: N-MORB and E-MORB [34]. N-MORB is more common, whereas E-MORB is considered less frequent and is characterized by the enrichment of incompatible elements and LREEs. They are predominantly found in certain MORB and near-seamount regions. Moreover, small amounts of basalt with E-MORB and ocean island basalt (OIB) characteristics have been found in modern back-arc basins [50]. N-MORB and OIB are considered two independent end-members, and E-MORB is not a separate component; rather, it is a mixture of varying degrees between N-MORB and OIB. Currently, there are two proposed models for the origin of E-MORB: one involving the interaction between mantle plume magma and N-MORB-depleted mantle magma, resulting in a gradual transition from OIB to E-MORB to N-MORB rock assemblages, with varying degrees of enrichment observed in E-MORB [51]; the other model suggests that E-MORB, which exhibits significant characteristics, occurs in areas far from mantle plumes, slow-spreading mid-ocean ridges, and back-arc basin tectonic settings, reflecting intrinsic heterogeneity in the mantle source region [52,53]. Ulrich et al. [54] proposed that binary mixtures of N-MORB and OIB sources accounted for the origin of E-MORB. Specifically, the cycling of the oceanic lithosphere is considered an important mechanism for creating enriched heterogeneous sources in the mantle, leading to the generation of rocks with OIB characteristics. In regions far from hotspot areas, the formation of E-MORB may involve two stages: the first stage includes the partial melting of subducted oceanic crust in the deep parts of subduction zones, forming an enriched mantle in the mantle wedge; the second stage involves the circulation of enriched mantle after subduction, which melts at mid-ocean ridges, resulting in the formation of E-MORB [54]. Considering the abundance of seamounts and oceanic islands on the seafloor, recycling into the upper mantle is a plausible process for generating E-MORB. Therefore, in the absence of hotspot-related processes, mixing between certain N-MORB sources and enriched components is considered the most comprehensive explanation for the variability in MORB enrichment.

From the normalized trace element patterns of the equilibrium melt, the samples exhibited characteristics between those of the MORB and OIB reference curves. Most trace element abundances were slightly higher than those in E-MORB, but lower than those in the OIB (Figure 13). Compared to primitive mantle rocks, except for a few large-ion lithophile elements (LILEs), incompatible elements do not show significant fractionation and exhibit characteristics between MORB and OIB. However, compared to E-MORB, the equilibrium melt exhibited enrichment of LREEs and LILEs and slight depletion in Nb, Zr, and Hf, but no significant enrichment in Th, indicating that magmatic activity may have experienced subduction, arguing against an important role of crustal contamination [55]. The concentrations of Ta and Nb in clinopyroxene are significantly lower than those in the crust (Nb = 8 ppm, Ta = 0.7 ppm) [56], indicating that the gabbroic magmas originated from a depleted mantle source. Discrimination using trace element ratios, such as La/Yb

vs. Nb/Yb and Th/Yb vs. Ta/Yb, can reflect variations in source material composition along the MORB–OIB sequence [4]. Figure 14a shows that the whole-rock composition of the Bingdaban gabbro and the equilibrium melt are scattered between N-MORB and E-MORB within the mantle array and are closer to the E-MORB source, suggesting that the mantle source represents a transition from depletion to minor enrichment. In addition, the participation of subduction components is shown in Figure 14b, indicating a subduction-modified depleted mantle source. Because there are no reports of contemporaneous mantle plume magmatism in the region, the enriched components in the Bingdaban E-MORB ophiolite are thought to be unrelated to the direct involvement of mantle plumes, but may be associated with the subduction and recycling of alkaline basalts from seamounts and oceanic islands.

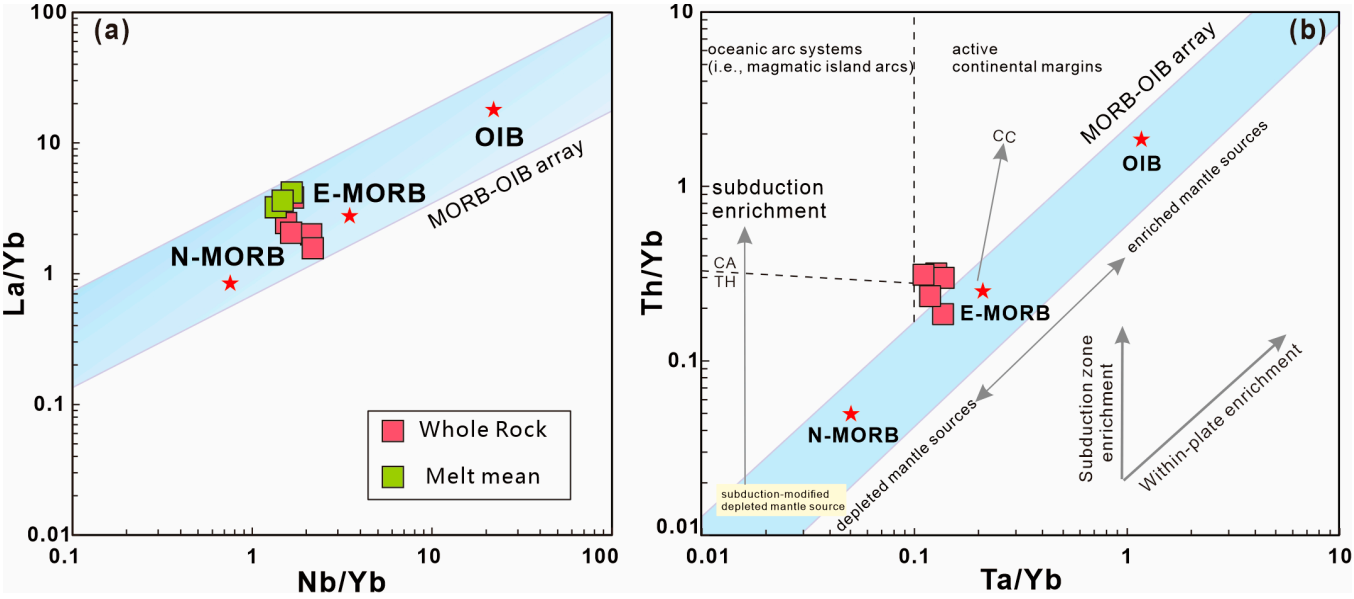

Figure 14. Trace element ratio discriminant diagrams for gabbro from Bingdaban. (**a**) La/Yb vs. Nb/Yb; (**b**) Ta/Yb vs. Th/Yb; N-MORB, E-MORB, and OIB compositions are from Sun and McDonough [34]. The mantle array and the calc-alkaline (CA) and tholeiitic (TH) boundaries for oceanic arc basalts are from Pearce [57]. Vectors: CC = crustal contamination.

5.6. Geodynamic Evolution

The Paleo-Tianshan Ocean, an important southern branch of the Paleozoic Paleo-Asian Ocean, records the evolution of the southern branch and is crucial for understanding the formation of the southernmost end of the CAOB [22,58]. Since the Early Paleozoic, the Paleo-Tianshan Ocean has been subducting beneath the northern margin of the Tarim Craton. Due to differences in tectonic positions, the Northern Tianshan tectonic zone developed into an Early Paleozoic multi-island ocean basin during the Middle Ordovician through rifting and rift basin formation, while the Southern Tianshan tectonic zone remained relatively stable and experienced tectonic environments of shallow marine or intercontinental basins [59]. After the formation of the Early Paleozoic multi-island ocean basin in Northern Tianshan, the oceanic crust subducted along the Aqikkuduk–Aibi Lake Fault from northeast to southwest. Further confirmation of the southward subduction mode of the Paleo-Tianshan Ocean is supported by extensive Early Paleozoic arc magmatism exposed along the northern margin of the Yili–Central Tianshan Block, whereas numerous ophiolites are distributed along the northern margin of Central Tianshan, including those in the Weiya, Gangou, and Bingdaban regions [6,7,11]. As the Paleo-Tianshan oceanic lithosphere continued to subduct beneath the Central Tianshan terrane, a back-arc basin (Southern Tianshan Ocean) formed between the Tarim and Central Tianshan during the Ordovician and Early Devonian [5,60]. As subduction continued, the OIB component was scraped off, while the

residual seamounts remained and continued to migrate with the subducting slab. Upon reaching a certain depth, fluid was released due to the dehydration of the slab, leading to the partial melting of the residual seamounts. The cycling of OIB components into the upper mantle under the influence of mantle convection resulted in their mixing with depleted mantle material, forming E-MORB sources through a binary mixing process (Figure 15). Considering the above discussion, the Bingdaban E-MORB gabbro likely originated in an initial oceanic basin stretching or an immature back-arc basin environment.

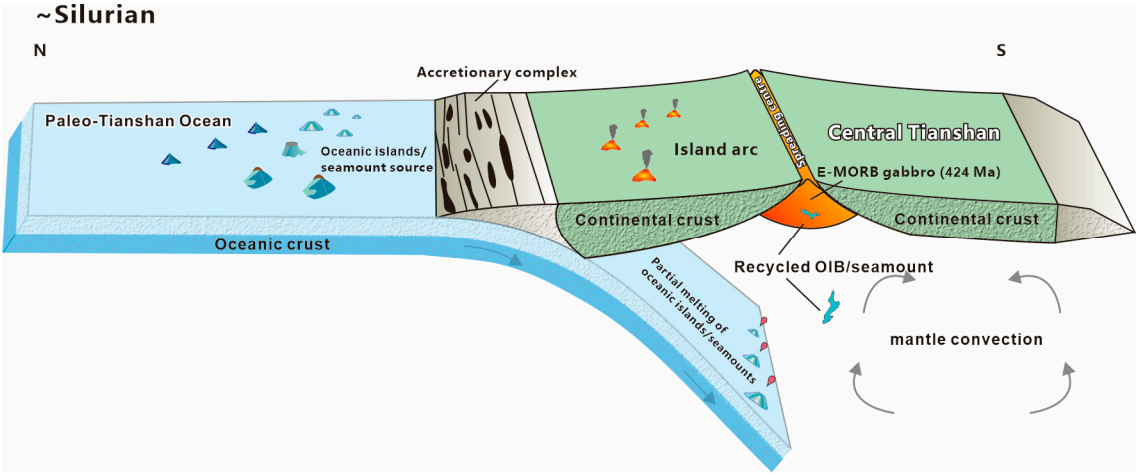

Figure 15. Sketch of enriched mid-ocean ridge basalt (E-MORB) genesis from the Bingdaban gabbro [28,54].

6. Conclusions

Based on field and petrological observations, and geochronological, whole-rock geochemical, and clinopyroxene chemical data, we reached the following conclusions:

1. The crystallization age of zircon in the Bingdaban gabbro was 424.3 ± 5.9 Ma, representing the Late Silurian age of the Bingdaban ophiolite formation.
2. The chemical composition of clinopyroxene in the Bingdaban gabbro indicates affinity for the subalkaline tholeiitic magma series. Along with magma evolution, clinopyroxene shows a decrease in $Mg^{\#}$ and a slight increase in FeO, indicating an evolutionary trend from Mg- to Fe-rich compositions.
3. Temperature and pressure estimations of the clinopyroxene indicate that the magmas were likely formed by high-temperature, low-pressure, shallow sources.
4. The melting model calculated from the clinopyroxene showed similarities to the host rock, reflecting the genetic characteristics of an E-MORB setting. The origin of the magma can be attributed to a depleted mantle source with the involvement of minor enriched mantle material, likely forming an initial oceanic basin or immature back-arc basin tectonic setting.

Supplementary Materials: The following supporting information can be downloaded at: https://www.mdpi.com/article/10.3390/min13091232/s1, Table S1. LA-ICP-MS U–Pb data for zircons from Bingdaban gabbro of the Central Tianshan; Table S2. Whole-rock major and trace element compositions of Bingdaban gabbro of the Central Tianshan; Table S3. Major element data and mineral end member calculation results for clinopyroxenes in Bingdaban gabbro from the Central Tianshan; Table S4. Trace element data for clinopyroxenes in Bingdaban gabbro from the Central Tianshan; Table S5. Partition coefficients (Kd) used in the calculations of equilibrium melts; Table S6. Temperatures and pressures calculated for clinopyroxenes in Bingdaban gabbro from the Central Tianshan.

Author Contributions: Conceptualization, Y.S. and Y.X.; methodology, Y.S.; formal analysis, Y.S., Y.X. and H.T.; investigation, Y.S., X.L. (Xijun Liu), Y.X., X.L. (Xiao Liu) and H.T.; data curation, Y.S., X.L. (Xijun Liu) and X.L. (Xiao Liu); writing—original draft, Y.S.; writing—review and editing, X.L. (Xijun

Liu) and Y.X.; supervision, X.L. (Xijun Liu); project administration, X.L. (Xijun Liu). All authors have read and agreed to the published version of the manuscript.

Funding: This study was supported financially by funds from the National Natural Science Foundation of China (92055208, 42203051), the Guangxi Science Innovation Base Construction Foundation (GuikeZY21195031), Natural Science Foundation of Guangxi, China (Nos. GuikeAD23026175, 2022GXNSFBA035538), the Fifth Bagui Scholar Innovation Project of Guangxi Province (to XU Jifeng), and the Innovation Project of Guangxi Graduate Education (YCBZ2023145). This is a contribution to "Xinjiang Tianchi Distinguished Expert" to Liu Xijun and Guangxi Key Mineral Resources Deep Exploration Talent Highland.

Data Availability Statement: Not Applicable.

Acknowledgments: We thank the journal editor and the three reviewers for their critical and constructive comments, which improved the earlier version of the manuscript.

Conflicts of Interest: The authors declare no conflict of interest.

References

1. Burke, K.; Dewey, J.F.; Kidd, W.S.F. World distribution of sutures—The sites of former oceans. *Tectonophysics* **1977**, *40*, 69–99. [CrossRef]
2. Dewey, J.F. Suture zone complexities: A review. *Tectonophysics* **1977**, *40*, 53–67. [CrossRef]
3. Dilek, Y.; Furnes, H. Ophiolite genesis and global tectonics: Geochemical and tectonic fingerprinting of ancient oceanic lithosphere. *Geol. Soc. Am. Bull.* **2011**, *123*, 387–411. [CrossRef]
4. Saccani, E. A new method of discriminating different types of post-Archean ophiolitic basalts and their tectonic significance using Th-Nb and Ce-Dy-Yb systematics. *Geosci. Front.* **2015**, *6*, 481–501. [CrossRef]
5. Wang, B.; Faure, M.; Shu, L.S.; Cluzel, D.; Charvet, J.; De Jong, K.; Chen, Y. Paleozoic tectonic evolution of the Yili Block, western Chinese Tianshan. *Bull. Soc. Geol. Fr.* **2008**, *179*, 483–490. [CrossRef]
6. Charvet, J.; Shu, L.S.; Laurent-Charvet, S. Paleozoic structural and geodynamic evolution of eastern Tianshan (NW China): Welding of the Tarim and Junggar Plates. *Episodes* **2007**, *30*, 162–186.
7. Shu, L.S.; Charvet, J.; Guo, L.Z.; Lu, H.F.; Laurent-Charvet, S. A large-scale Palaeozoic dextral ductile strike-slip zone: The Aqqikkudug-Weiya zone along the northern margin of the central Tianshan belt, Xinjiang, NW China. *Acta Geol. Sin.* **1999**, *2*, 148–162.
8. Wang, B.; Shu, L.S.; Faure, M.; Jahn, B.M.; Cluzel, D.; Charvet, J.; Chung, S.L.; Meffre, S. Paleozoic tectonics of the southern Chinese Tianshan: Insights from structural, chronological and geochemical studies of the Heiyingshan ophiolitic mélange (NW China). *Tectonophysics* **2011**, *497*, 85–104. [CrossRef]
9. Windley, B.F.; Allen, M.B.; Zhang, C.; Zhao, Z.Y.; Wang, G.R. Paleozoic accretion and Cenozoic redeformation of the Chinese Tien shan Range, central Asia. *Geology* **1990**, *18*, 128–131. [CrossRef]
10. Ma, Z.P. *Research on Ophiolites in Tianshan and Its Adjacent Areas and Evolution of Paleozoic Ocean Basins*; Northwest University: Kirkland, DC, USA, 2007; (In Chinese with English Abstract).
11. Dong, Y.P.; Zhang, G.W.; Zhou, B.W.; Luo, J.H.; Zhang, C.L.; Xia, L.Q.; Xu, X.Y.; Li, X.M. *Determination and Tectonic Significance of Bingdaban Ophiolitic Mellitic Rocks in the Northern Margin of Central Tianshan*; Science in China Press: Beijing, China, 2005; pp. 552–560, (In Chinese with English Abstract).
12. Liu, X.J.; Zhang, Z.G.; Xu, J.F.; Xiao, W.; Shi, Y.; Gong, X.; Tan, Z.J.; Li, R. The youngest Permian Ocean in Central Asian Orogenic Belt: Evidence from Geochronology and Geochemistry of Bingdaban Ophiolitic Mélange in Central Tianshan, northwestern China. *Geol. J.* **2020**, *55*, 2062–2079. [CrossRef]
13. Nisbet, E.G.; Pearce, J.A. Clinopyroxene composition in mafic lavas from different tectonic settings. *Contrib. Miner. Pet.* **1977**, *63*, 149–160. [CrossRef]
14. Xiao, X.C.; Tang, Y.Q.; Feng, Y.M. *Tectonic Evolution of the Northern Xinjiang and Its Adjacent Regions*; Geological Publishing House: Beijing, China, 1992; pp. 104–123.
15. Gao, J.; Long, L.L.; Klemd, R.; Qian, Q.; Liu, D.Y.; Xiong, X.M.; Su, W.; Liu, W.; Wang, Y.T.; Yang, F.Q. Tectonic evolution of the South Tianshan orogen and adjacent regions, NW China: Geochemical and age constraints of granitoid rocks. *Int. J. Earth Sci.* **2009**, *98*, 1221–1238. [CrossRef]
16. Long, L.L.; Gao, J.; Klemd, R.; Beier, C.; Qian, Q.; Zhang, X.; Wang, J.B.; Jiang, T. Geochemical and geochronological studies of granitoid rocks from the Western Tianshan Orogen: Implications for continental growth in the southwestern Central Asian Orogenic Belt. *Lithos* **2011**, *126*, 321–340. [CrossRef]
17. Qian, Q.; Gao, J.; Klemd, R.; He, G.Q.; Song, B.; Liu, D.Y.; Xu, R.H. Early Paleozoic tectonic evolution of the Chinese South Tianshan Orogen: Constraints from SHRIMP zircon U–Pb geochronology and geochemistry of basaltic and dioritic rocks from Xiate, NW China. *Int. J. Earth Sci.* **2009**, *98*, 551–569. [CrossRef]

18. Wang, X.S.; Gao, J.; Klemd, R.; Jiang, T.; Li, J.L.; Zhang, X.; Tan, Z.; Li, L.; Zhu, Z. Geochemistry and geochronology of the Precambrian high-grade metamorphic complex in the Southern Central Tianshan ophiolitic mélange, NW China. *Precambrian Res.* **2014**, *254*, 129–148. [CrossRef]
19. Alexeiev, D.V.; Biske, Y.S.; Wang, B.; Djenchuraeva, A.V.; Getman, O.F.; Aristov, V.A.; Kröner, A.; Liu, H.; Zhong, L. Tectono-stratigraphic framework and Palaeo-zoic evolution of the Chinese South Tianshan. *Geotectonics* **2015**, *49*, 93–122. [CrossRef]
20. Allen, M.B.; Windley, B.F.; Zhang, C. Paleozoic collisional tectonics and magmatism of the Chinese Tien shan, Central Asia. *Tectonophysics* **1993**, *220*, 89–115. [CrossRef]
21. Zhang, L.; Chen, H.Y.; Liu, C.F.; Zheng, Y. Ore genesis of the Saridala gold deposit, Western Tianshan, NW China: Constraints from fluid inclusion, S-Pb isotopes and 40Ar/39Ar dating. *Ore. Geol. Rev.* **2018**, *100*, 63–76. [CrossRef]
22. Şengör, A.M.C.; Natal'in, B.A.; Burtman, V.S. Evolution of the Altaid tectonic collage and Palaeozoic crustal growth in Eurasia. *Nature* **1993**, *364*, 299–307. [CrossRef]
23. Chen, G.W.; Yang, J.X.; Liu, R.; Wang, L.X.; Wang, K. Geochemistry of mafic volcanics in the Bayingou ophiolitic mélange, Western Tianshan, NW China: Implications for magma genesis and tectonic setting. *Lithos* **2020**, *352–353*, 105292. [CrossRef]
24. Dong, Y.P.; Zhou, D.W.; Zhang, G.W.; Zhao, X.; Luo, J.H.; Xu, J.G. Geology and geochemistry of the Gangou ophiolitic melange at the northern margin of the Middle Tianshan Belt. *Acta Pet. Sin.* **2006**, *22*, 49–56, (In Chinese with English Abstract).
25. Zhong, L.L.; Wang, B.; Shu, L.S.; Liu, H.S.; Mu, L.X.; Ma, Y.Z.; Zhai, Y.Z. Structural overprints of Early Paleozoic arc-related intrusive rocks in the Chinese Central Tianshan: Implications for Paleozoic accretionary tectonics in SW Central Asian Orogenic Belts. *J. Asian Earth Sci.* **2015**, *113*, 194–217. [CrossRef]
26. XBGMR. 1:200,000 Geological Map. Baluntai Sheet (K-45-10) 1977. Accessed on: 10 June 2021. 10 June.
27. Chen, X.Y.; Wang, Y.J.; Sun, L.H.; Fan, W.M. Zircon SHRIMP U-Pb dating of the granitic gneisses from Bingdaban and Laserdundaban (Tianshan Orogen) and their geological significances. *Geochimica* **2009**, *38*, 424–431, (In Chinese with English Abstract).
28. Xiao, W.J.; Windley, B.F.; Allen, M.B.; Han, C.M. Paleozoic multiple accretionary and collisional tectonics of the Chinese Tianshan orogenic collage. *Gondwana Res.* **2013**, *23*, 1316–1341. [CrossRef]
29. Liu, X.J.; Xu, J.F.; Castillo, P.R.; Xiao, W.J.; Shi, Y.; Zhang, Z.; Wang, X.-C.; Ao, S.; Wang, B.; Hu, R.; et al. Long-lived low Th/U Pacific-type isotopic mantle domain: Constraints from Nd and Pb isotopes of the Paleo-Asian Ocean mantle. *Earth Planet Sci. Lett.* **2021**, *567*, 117006. [CrossRef]
30. Song, Y.J.; Liu, X.J.; Xiao, W.J.; Gong, X.H.; Liu, X.; Xiao, Y.; Zhang, Z.G.; Liu, P.D. Tectonic evolution of circum-Rodinia subduction: Evidence from Neoproterozoic A-type granitic magmatism in the Central Tianshan Block, northwest China. *Precambrian Res.* **2023**, *387*, 106976. [CrossRef]
31. Ludwig, K. *User's Manual for Isoplot 3.00: A Geochronological Toolkit for Microsoft Excel*; Berkeley Geochronology Center: Berkeley, CA, USA, 2003; (Special Publications No. 4).
32. Middlemost, E.A.K. Naming materials in the magma/igneous rock system. *Earth-Sci. Rev.* **1994**, *37*, 215–224. [CrossRef]
33. Miyashiro, A. Volcanic rock series in island arcs and active continental margins. *Am. J. Sci.* **1974**, *274*, 321–355. [CrossRef]
34. Sun, S.S.; McDonough, W.F. Chemical and isotopic systematics of oceanic basalts: Implications for mantle composition and processes. *Geol. Soc. Spec. Publ.* **1989**, *42*, 313–345. [CrossRef]
35. Morimoto, N. Nomenclature of pyroxenes. *Miner. Pet.* **1988**, *39*, 55–76. [CrossRef]
36. Qiu, J.X.; Liao, Q.A. Petrogenesis and Cpx mineralchemistry of Cenozoic basalts from Zhejiang and Fujian of eastern China. *Volcanol. Miner. Resour.* **1996**, *17*, 16–25, (In Chinese with English Abstract).
37. Kou, C.H.; Liu, Y.X.; Li, T.D.; Ding, X.Z.; Zhang, H.; Liu, Y. Petrogenesis and tectonic implications of the neoproterozoic mafic-ultramafic rocks in the western Jiangnan Orogen: Insights from in situ analysis of clinopyroxenes. *Lithos* **2021**, *392–393*, 106156. [CrossRef]
38. Zou, J.X.; Liu, X.F.; Deng, J.H.; Li, C.H.; Huang, Y.P.; Dong, Y.; Yi, L.W. Mineralogical composition characteristics and geological significance of the clinopyroxene from ultrabasic-basic rocks at Luoji Village, Shangri-la County, Yunnan Province. *Acta Pet. Miner.* **2012**, *31*, 701–711, (In Chinese with English Abstract).
39. Le Bas, M.J. The role of aluminum in igneous clinopyroxenes with relation to their parentage. *Am. J. Sci.* **1962**, *260*, 267–288. [CrossRef]
40. Putirka, K.D. Thermometers and barometers for volcanic systems. *Rev. Miner. Geochem.* **2008**, *69*, 61–120. [CrossRef]
41. Putirka, K.D.; Mikaelian, H.; Ryerson, F.; Shaw, H. New clinopyroxene-liquid thermobarometers for mafic, evolved, and volatile-bearing lava compositions, with applications to lavas from Tibet and the Snake River Plain, Idaho. *Am. Miner.* **2003**, *88*, 1542–1554. [CrossRef]
42. Irving, A.J.; Frey, F.A. Trace element abundances in megacrysts and their host basalts: Constraints on partition coefficients and megacryst genesis. *Geochim. Cosmochim. Acta* **1984**, *48*, 1201–1221. [CrossRef]
43. Liotard, J.M.; Briot, D.; Boivin, P. Petrological and geochemical relationships between pyroxene megacrysts and associated alkali-basalts from Massif Central (France). *Contrib. Miner. Pet.* **1988**, *98*, 81–90. [CrossRef]
44. Wood, B.J.; Blundy, J.D. A predictive model for rare earth element partitioning between clinopyroxene and anhydrous silicate melt. *Contrib. Miner. Pet.* **1997**, *129*, 166–181. [CrossRef]
45. Neave, D.A.; Putirka, K.D. A new clinopyroxene-liquid barometer, and implications for magma storage pressures under Icelandic rift zones. *Am. Miner.* **2017**, *102*, 777–794. [CrossRef]

46. Kinzler, R.J. Melting of mantle peridotite at pressures approaching the spinel to garnet transition: Application to Mid-Ocean Ridge basalt petrogenesis. *J. Geophys. Res.* **1997**, *102*, 853–874. [CrossRef]
47. Hart, S.R.; Dunn, T. Experimental cpx/melt partitioning of 24 trace elements. *Contr. Mineral. Petrol.* **1993**, *113*, 1–8. [CrossRef]
48. Arevalo, R.; McDonough, W.F. Chemical variations and regional diversity observed in MORB. *Chem. Geol.* **2010**, *271*, 70–85. [CrossRef]
49. Wang, Z.X.; Li, C.L.; Nikolai, P.; Elena, I.; Yu, X.Q.; Zhou, G.; Xiao, W.F.; Han, S.Q.; Zailabidin, H.; Nurgazy, T.; et al. Tectonic division and Paleozoic ocean-continent transition in Western Tianshan Orogen. *Geol. China* **2017**, *44*, 623–641, (In Chinese with English Abstract).
50. Liu, X.J.; Xu, J.F.; Wang, S.Q.; Hou, Q.Y.; Bai, Z.H.; Lei, M. Geochemistry and dating of E-MORB type mafic rocks from Dalabute ophiolite in West Junggar, Xinjiang and geological implications. *Acta Petrol. Sin.* **2009**, *25*, 1373–1389, (In Chinese with English Abstract).
51. Guo, A.L.; Zhang, G.W.; Sun, Y.G.; Zheng, J.K.; Liu, Y.; Wang, J.Q. Geochemical and spatial distribution characteristics of OIB and MORB in the Animaqing ophiolitic belt: Evidence of hot spot tectonics in the ancient ocean ridge of Maji snow mountain. *Sci. China* **2006**, *36*, 618–629, (In Chinese with English Abstract).
52. Donnelly, K.E.; Goldstein, S.L.; Langmuir, C.H.; Spiegelman, M. Origin of enriched ocean ridge basalts and implications for mantle dynamics. *Earth Planet Sci. Lett.* **2004**, *226*, 347–366. [CrossRef]
53. Schilling, J.-G. Iceland mantle plume: Geochemical study of Reykjanes Ridge. *Nature* **1973**, *242*, 565–571. [CrossRef]
54. Ulrich, M.; Hémond, C.; Nonnotte, P.; Jochum, K.P. OIB/seamount recycling as a possible process for E-MORB genesis. *Geochem. Geophys. Geosyst.* **2012**, *13*, 1–24. [CrossRef]
55. Wang, J.; Su, Y.P.; Zheng, J.P.; Belousova, E.A.; Chen, M.; Dai, H.K.; Zhou, X. Petrogenesis of early Carboniferous bimodal-type volcanic rocks from the Junggar Basin (NW China) with implications for Phanerozoic crustal growth in Central Asian Orogenic Belt. *Gondwana Res.* **2021**, *89*, 220–237. [CrossRef]
56. Rudnick, R.; Gao, S. Composition of the continental crust. *Treatise Geochem.* **2003**, *3*, 1–64. [CrossRef]
57. Pearce, J.A. The role of sub-continental lithosphere in magma genesis at destructive plate margins. In *Continental Basalts and Mantle Xenoliths*; Hawkesworth, C.J., Norry, M.J., Eds.; Shiva: Nantwich, UK, 1983; pp. 230–249.
58. Windley, B.F.; Alexeiev, D.; Xiao, W.J.; Kröner, A.; Badarch, G. Tectonic models for accretion of the Central Asian Orogenic Belt. *J. Geol. Soc.* **2007**, *164*, 31–47. [CrossRef]
59. Wang, J.R.; Chen, W.F.; Zhang, Q.; Jiao, S.T.; Yang, J.; Pan, Z.J.; Wang, S.H. Preliminary research on data mining of NMORBand E-MORB: Discussion on method of the basalt discrimination diagrams and the character of MORB's mantle source. *Acta Petrol. Sin.* **2017**, *33*, 993–1005, (In Chinese with English Abstract).
60. Charvet, J.; Shu, L.S.; Laurent-Charvet, S.; Wang, B.; Faure, M.; Cluzel, D.; Chen, Y.; De Jong, K.D. Palaeozoic tectonic evolution of the Tianshan belt, NW China. *Sci. China Earth Sci.* **2011**, *54*, 166–184. [CrossRef]